

# EBSDB Study on Processing Domain Parameters of Oxide Dispersion Strengthened 18Cr Ferritic Steel

Manmath Kumar Dash, S. Saroja, Rahul John, R. Mythili, and Arup Dasgupta

(Submitted July 16, 2018; in revised form September 15, 2018; published online December 17, 2018)

This paper presents the results of an experimental study aimed to identify hot working domains in oxide dispersion strengthened (ODS) 18Cr ferritic steel over a wide range of temperatures (1323–1473 K) and strain rates (0.01–10 s<sup>-1</sup>). The experimental data were obtained by uniaxial compression test using the Gleeble-1500D simulator in this range of temperature and strain rate. An inverse relationship with temperature and positive strain rate sensitivity associated with dynamic recovery and recrystallization, which is influenced by temperature and strain rate, was derived from the flow stress. Based on the processing map generated at 0.5 true strain, using rate dynamic material model (DMM) approach and the calculated instability parameter ( $\xi(\dot{\epsilon}) > 0$ ), the optimum processing domain has been determined for this steel. The most favorable processing parameters are found in the temperature ranges of 1350–1450 K with a strain rate of 0.01 s<sup>-1</sup> and 1473 K with a strain rate 0.1 s<sup>-1</sup> with peak efficiency of 30 and 35%, respectively. The material flow behavior was studied using scanning electron microscopy (SEM)-based EBSD microstructural characterization. The steel subjected to 1323 K at high strain rate 10 s<sup>-1</sup> in the low-efficiency workability region showed low aspect ratio as compared to the elongated bamboo-like initial microstructure; however, minimum strain rate (0.01 s<sup>-1</sup>) showing that localized slip/shearing is the key mechanism and fiber texture studied from the intensity distribution of inverse pole figure showed the presence of significant amount of  $\theta$ -fibers. In contrast, dynamic recrystallization dominated at higher efficiency region in the safe domain of processing map and  $\gamma$ -fiber texture was evident in the specimen deformed at 1373 and 1473 K with strain rate of 0.01 and 0.1 s<sup>-1</sup>, respectively, which is responsible for the change in the initial  $\langle 110 \rangle$ /ED  $\alpha$ -fiber texture.

**Keywords** EBSD, fiber texture, processing, stainless steel

## 1. Introduction

Aggressive service condition such as high-energy neutron irradiation at high-temperature poses a strong challenge in selection of materials for Gen IV nuclear reactors (Ref 1–3). Ferritic–martensitic steels with a bcc structure are considered to be superior to austenitic steels for high damage levels exceeding 155 dpa, due to their excellent void swelling resistance (Ref 4). However, their high-temperature creep and corrosion/oxidation properties are to be improved for good performance as core structural materials. In this context, addition of oxide dispersoids in dispersion strengthened high (> 12%) Cr ferritic steels provides excellent creep properties at elevated temperature as well as swelling resistance, due to the effective pinning of dislocations (Ref 8–10). This makes them potential candidates for cladding in fast breeder reactors and first wall in fusion reactors (Ref 5–7). Besides creep and swelling resistance, increasing Cr content helps in enhancement

of corrosion/oxidation properties is desirable to reprocess the spent fuel (Ref 11–13). These steels are fabricated by a powder metallurgical route, wherein mechanical alloying is followed by various sequences of cold or warm working and annealing treatments (Ref 14). However, the anisotropic morphological microstructure that forms during unidirectional fabrication induces severe anisotropy in mechanical properties and remains a point of concern for their final applications (Ref 6, 15, 16).

During thermomechanical treatments, the steel undergoes a variety of metallurgical changes like dynamic recovery and recrystallization as well as work hardening and flow instability (Ref 18, 19). The resultant microstructure influences the mechanical properties and performance of the final product during service exposure. In order to design an appropriate microstructure, it is necessary to optimize the high-temperature deformation domain through generation of processing maps and in this context the dynamic material models (DMMs) are useful (Ref 20, 21).

Several studies are reported on processing parameters for various materials such as austenitic stainless steels (Ref 22–24) and 9Cr–1Mo/9Cr ODS steels (Ref 25, 26) based on their high-temperature deformation behavior, and the mechanisms have also been reported. Few studies are available on high (> 12%) Cr ODS ferritic steels, wherein the microstructural modification is achieved through various thermomechanical treatments (Ref 17, 27). In the present study, processing map of an 18Cr ODS ferritic steel is generated by hot compression test using Gleeble simulator to identify the hot working parameters. The evolution of microstructure and microtexture in the processing domains has been studied using the SEM based Electron Backscatter Diffraction technique.

**Manmath Kumar Dash, S. Saroja, R. Mythili, and Arup Dasgupta**, Metallurgy and Materials Group, Indira Gandhi Centre for Atomic Research, Kalpakkam, India; and IGCAR, HBNI, Kalpakkam 603102, India; **Rahul John**, Indian Institute of Technology Madras, Chennai 600036, India. Contact e-mail: manmath@igcar.gov.in.

## 2. Experimental Procedure

### 2.1 Material and Specimen Preparation

18Cr ODS ferritic steel used in the present work was obtained by a powder metallurgical route followed by consolidation using hot extrusion (HE) process in collaboration with International Advanced Research Centre for Powder Metallurgy and New Materials (ARCI) and Nuclear Fuel Complex (NFC), Hyderabad.

Pre-alloyed steel powder of nominal composition Fe-18Cr-2W-0.01C-0.2Ti of average particle size  $\sim 100 \mu\text{m}$  was mechanically blended with  $0.35\text{Y}_2\text{O}_3$  (by weight) powder of  $\sim 40 \text{ nm}$  size in an attritor mill under argon atmosphere following optimized milling conditions. Details of the process are given elsewhere (Ref 28). The powders packed in mild steels cans of  $\sim 72 \text{ mm}$  diameter were upset forged under pressure of 800 MPa at 1323 K (1050 °C) to produce forged billets. The forged billets were extruded to a diameter of 24 mm at 1423 K with extrusion speed 25-30 m/s at a pressure of  $\sim 620 \text{ MPa}$ .

Cylindrical specimens of  $9 \pm 0.1 \text{ mm}$  height and  $6 \pm 0.1 \text{ mm}$  diameter were fabricated from the extruded rod for the hot compression tests using Gleeble simulator. During compression testing at high temperatures, it is reported that the contact surface experiences a higher stress than the center (Ref 29). This means a higher possibility of sticking to the die, which could lead to high strain level and increase in the friction coefficient as well. Application of lubricant helps in reducing this. Hence, the flat faces of the cylindrical samples were grooved with concentric circles up to 0.5 mm depth for withholding the lubricant to reduce the effect of friction (Ref 30). The thermocouple was welded with specimen surface for a precise temperature measurement during testing.

### 2.2 Hot Compression Test

The Gleeble-1500D simulator was used to conduct the hot compression tests. The 'Gleeble' machine typically provides controlled rate of heating and cooling of specimens. The mainframe controller in the system keeps the true strain rate constant during deformation. The axisymmetric compression test is carried out by compressing the cylindrical sample between two parallel platens, and the displacements of the platens impose the axial compression. Specimens were held for 5 min at the testing temperature prior to the deformation process to attain equilibrium. The specimens were deformed to a maximum strain of 50% at a constant true strain rate in the range  $0.01\text{-}10 \text{ s}^{-1}$  in the temperature range of 1323 K (1050 °C) to 1473 K (1250 °C) at intervals of 50 K, followed by immediate to suppress any diffusional transformation during cooling. A total of 16 specimens were used for each of the four strain rate and four temperature conditions. The Gleeble 1500D contains direct resistance heating system and heats specimens at rates of up to 10,000 °C/s, or can hold steady-state equilibrium temperatures. Supplementary thermocouples and infrared pyrometer have been attached for precise feedback control of temperatures for the specimen. In comparison with conventional furnace equipped machines, the Gleeble systems can run thermal tests typically 3-10 times faster, because of the unique high-speed heating method. The grips that hold the specimen are made with high thermal conductivity and enhance the capability of high cooling rates in Gleeble 1500D. An

additional water quench system has also been provided to attain further high cooling rates for the specimen and to avoid temperature gradation.

The dimensions of each specimen were measured after hot compression test including the diameter of the top ( $d_{\text{min}}$ ) and bottom ( $d_{\text{min}}$ ) surfaces, maximum diameter ( $d_{\text{max}}$ ) in barreled section and the specimen height ( $h$ ). Five measurements were carried out for each specimen using a digital Vernier Caliper with resolution 0.01 mm. Dimensions of the specimen 1-16 are listed in Table 1 which shows the variations are negligible for different test conditions.

### 2.3 SEM/EBSD Characterization

The specimens were sectioned using a precision cutting machine along the longitudinal direction of hot compression testing geometry to obtain the mid-thickness which is known to be the maximum deformation zone. Microstructure and microtexture analysis was carried out using EBSD attached to FEI Helios Nanolab 600i Field Emission Scanning Electron Microscope (FE-SEM) at 20 kV at appropriate magnifications to include reasonable number of grains using a scan step of  $0.05 \mu\text{m}$ . The standard metallographic procedure was carried out followed by final electropolishing in '20% Perchloric acid + 80% methanol' electrolyte at 283-287 K (10-15 °C) and 15 V. The TSL-OIM™ software was used to analyze the microtexture scan data. The as-extruded and uniaxial compression test are in line with axisymmetric products, and the crystal orientation described by inverse pole figure distribution map in one set of Miller indices  $[uvw]$  has been used to indicate the resultant crystallographic direction which is parallel to the sample axis (Ref 31). The extent of preferred orientation is approximated from the inverse pole figures by harmonic series expansion method evaluated with a tolerance angle criterion of  $5^\circ$  (Ref 32).

## 3. Results and Discussion

### 3.1 Characterization of Hot Extruded Steel

Grain boundary distribution along the extruded direction in 'as-extruded' sample is superimposed on the EBSD crystal orientation map in Fig. 1. The microstructure exhibits elongated grains with an average aspect ratio of 1.6, and the maximum dimensions of  $\sim 0.8 \pm 0.2$  and  $\sim 2 \pm 0.5 \mu\text{m}$  in the transverse and longitudinal direction, respectively. The black and gray lines in the microstructure represent the low ( $2^\circ\text{-}15^\circ$ ) and high ( $> 15^\circ$ )-angle boundaries, respectively. A close look shows a network of low-angle boundaries contained within the high-angle boundaries. The low-angle boundary networks indicate an intragrain rotation in the partially recovered microstructure, which is attributed to dynamic recovery during the extrusion process, which are the most common deformation and annealing mechanism at high temperatures (Ref 33, 34). Further, the orientation map suggests the existence of a preferential crystallographic plane normal to  $\langle 110 \rangle$  along the extrusion direction, which has been confirmed by the analysis of the inverse pole figure (IPF) (Fig. 1b). The analysis of IPF also shows a strong contribution of  $\langle 110 \rangle$  fiber texture along the extruded direction which is attributed to the deformation induced texture, and it is reported as a typical behavior of high Cr ( $> 12\%$ ) ferritic ODS steels (Ref 35).

**Table 1** Dimensions of pre- and post-hot compression tested specimen

Test condition	Specimen dimension				
	Initial diameter, mm	Initial height, mm	Post-hot compression tested specimen		
			$d_{min}$ , mm	$d_{max}$ , mm	Height, mm
1050 K/0.01 s <sup>-1</sup>	5.99	9.01	7.12	7.72	6.10
1050 K/0.1 s <sup>-1</sup>	6.00	8.95	7.10	7.70	5.80
1050 K/1 s <sup>-1</sup>	6.01	8.94	7.10	7.70	5.74
1050 K/10 s <sup>-1</sup>	5.98	8.98	7.14	7.68	5.74
1100 K/0.01 s <sup>-1</sup>	6.01	8.99	7.06	7.76	5.84
1100 K/0.1 s <sup>-1</sup>	5.99	8.98	7.04	7.78	5.82
1100 K/1 s <sup>-1</sup>	6.00	8.99	7.08	7.74	5.86
1100 K/10 s <sup>-1</sup>	6.00	8.98	7.08	7.70	6.02
1150 K/0.01 s <sup>-1</sup>	6.01	8.97	7.12	7.78	5.70
1150 K/0.1 s <sup>-1</sup>	5.99	8.99	7.08	7.80	5.88
1150 K/1 s <sup>-1</sup>	6.00	9.00	7.10	7.82	5.72
1150 K/10 s <sup>-1</sup>	6.01	8.96	7.10	7.80	5.88
1200 K/0.01 s <sup>-1</sup>	6.00	8.98	7.06	7.92	5.88
1200 K/0.1 s <sup>-1</sup>	6.01	8.98	7.08	7.90	5.78
1200 K/1 s <sup>-1</sup>	6.00	9.01	7.08	7.88	5.76
1200 K/10 s <sup>-1</sup>	6.00	8.98	7.12	7.88	5.74

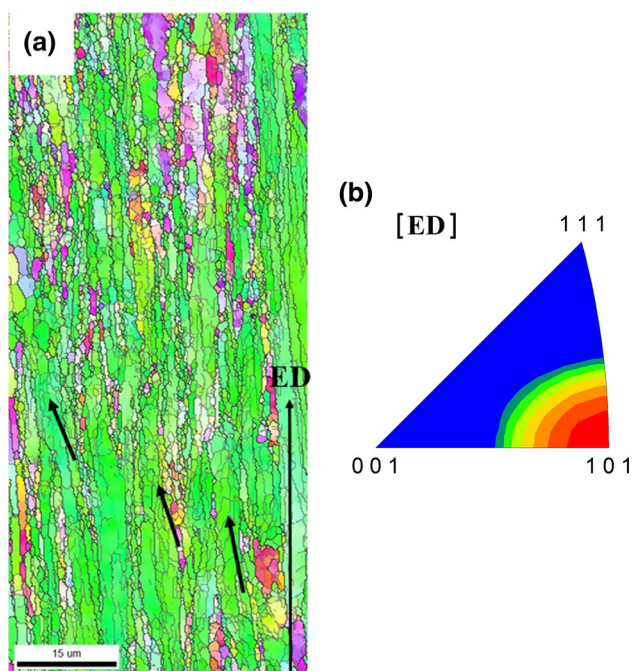


**Fig. 1** (a) Grain boundary distribution (Gray— $2^{\circ}$ – $15^{\circ}$  marked arrow, Black— $> 15^{\circ}$ ) superimposed on the EBSD crystal orientation map and (b) inverse pole figure from the longitudinal section of hot extruded rod of 18Cr ODS ferritic steel

### 3.2 Effect of Temperature and Strain Rate on Flow Stress

Figure 2 shows the experimental flow curves of the 18Cr ODS steel compression tested in a range of temperatures (1323–1473 K) and strain rates ( $0.01$ – $10$  s<sup>-1</sup>). Based on Table 1 where the dimensional changes are negligible it is assumed that deformation is homogeneous during compression test. The flow stress characteristics are observed to vary with test temperature and strain rate. A sharp increase in flow stress is observed at all temperatures and strain rates in the initial stages of deformation due to strain hardening phenomenon. However, beyond a true

strain value of 0.2, saturation or decrease in flow stress was observed, which is attributed to the softening due to dynamic recovery and recrystallization (Ref 26). At 1323 K, at strain rate  $\geq 0.1$  s<sup>-1</sup> a mild increase in flow stress with strain is observed (Fig. 2(a)). This is attributed to higher work hardening rate due to deformation at low-temperature and high strain rate.

Flow stress curves show a dominant softening behavior at low strain rates of  $\leq 0.1$  s<sup>-1</sup> at high temperatures of 1373–1473 K, suggesting recovery process and a steady-state behavior of the flow stress curves implies a balance between work hardening and thermal softening. This behavior is attributed to dynamic recovery which is characteristic of high Stacking Fault Energy (SFE) materials. The flow curve determined at 1373–1473 K, at a strain rate of  $0.01$  s<sup>-1</sup> suggests the occurrence of dynamic recrystallization, characteristic of the high temperature of deformation (Ref 36).

Although the characteristics of true stress–strain curves qualitatively indicate dynamic recrystallization (Ref 37), Poliak and Jonas have reported a point of inflection in the relationship of work hardening rate ( $\theta$ ) with stress ( $\sigma$ ) (Ref 36, 38, 39). Since,  $d(\ln\theta)/d\varepsilon = d\theta/d\sigma$ , an inflection point is also expected in the plot of  $\ln(\theta)$  as a function of  $\varepsilon$  which is a signature of dynamic recrystallization (Ref 40). The plot of  $\ln(\theta)$  versus  $\varepsilon$  at 1373 K with strain rate of  $0.01$  s<sup>-1</sup> is shown in Fig. 3. A sharp point of inflection in Fig. 3 thus substantiates the event of dynamic recrystallization above the temperature  $> 1373$  K in this material which in corroboration with the fact that observed in Fig. 2.

However, the experimental true stress–strain curves reflect the complex interplay of concurrently operating phenomena of work hardening and softening processes during high-temperature deformation and annealing. The identification of various workability regimes from the predicted flow stress using constitutive equations is explained in the subsequent section.

### 3.3 Hot Deformation Constitutive Equations

The analysis and simulation of the flow behavior can be predicted using constitutive equations for the material. The

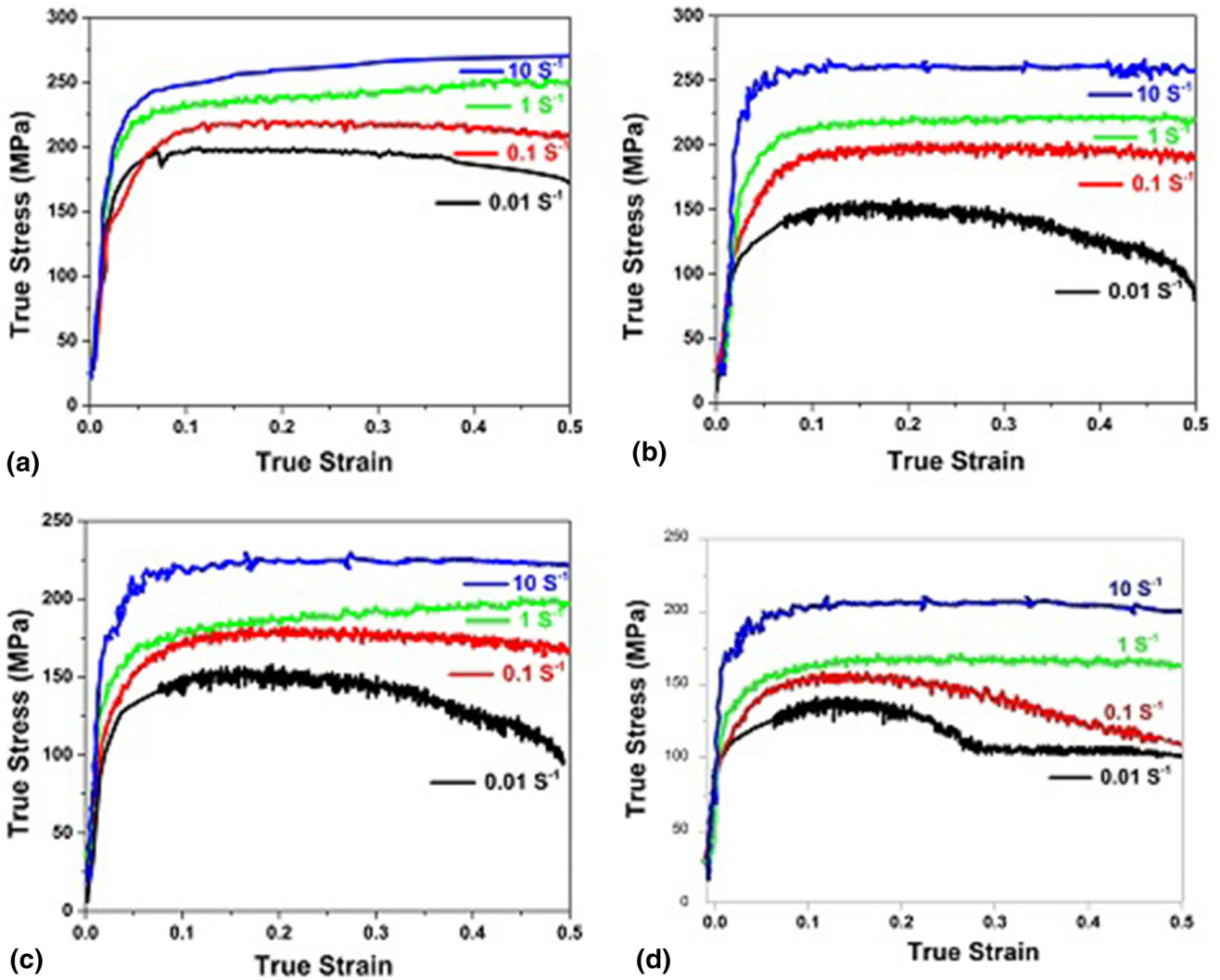


Fig. 2 True stress vs. true strain plots obtained by hot compression test for strain rates in the range of 0.01-10 s<sup>-1</sup> at temperatures of (a) 1323, (b) 1373, (c) 1423 and (d) 1473 K

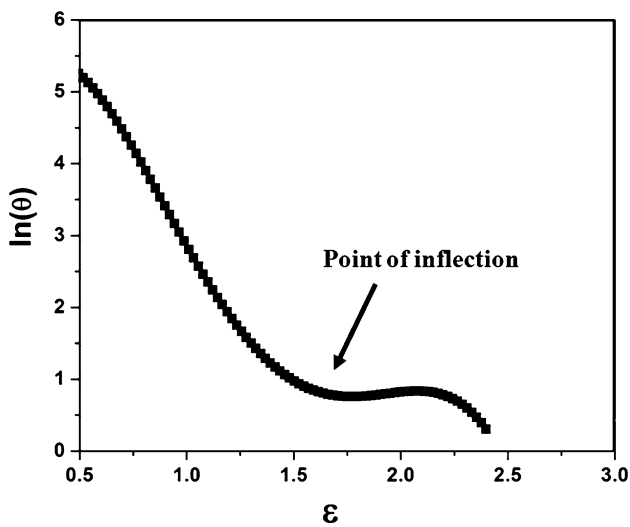


Fig. 3 Variation of work hardening rate ( $\ln \theta$ ) and strain ( $\epsilon$ ) of 18Cr ODS ferritic steel at 1373 K with strain rate of 0.01 s<sup>-1</sup>

Arrhenius equation is used to derive the correlation between flow stress and strain rate during high-temperature deformation (Ref 41), and the constitutive behavior can be explained as follows (Ref 26, 42-45):

$$\dot{\epsilon} = A_1 \sigma^{n_1} \exp\left[-\frac{Q}{RT}\right] \quad (\text{Eq 1})$$

$$\dot{\epsilon} = A_2 \exp(\beta\sigma) \exp\left[-\frac{Q}{RT}\right] \quad (\text{Eq 2})$$

$$\dot{\epsilon} = A[\sinh(\alpha\sigma)]^n \exp\left[-\frac{Q}{RT}\right] \quad (\text{Eq 3})$$

where Eq 1 and 2 correspond to the power exponent relationship in the low- and high-stress conditions, respectively, whereas Eq 3 represents sine relationship for all stress conditions, and therein  $\dot{\epsilon}$  is the strain rate,  $\sigma$  is the flow stress,  $T$  and  $Q$  are the temperature and activation energy during deformation, respectively,  $R$  is the gas constant (8.31 J mol<sup>-1</sup> K<sup>-1</sup>) and  $A_1$ ,  $A_2$ ,  $A$ ,  $n_1$ ,  $n$ ,  $\alpha$ , and  $\beta$  are denoted for material constants. Further, Eq 1-3 can be rewritten in the following way:

$$\ln \dot{\epsilon} = n_1 \ln \sigma + \ln A_1 - Q/(RT) \quad (\text{Eq 4})$$

$$\ln \dot{\epsilon} = \beta \sigma + \ln A_2 - Q/(RT) \quad (\text{Eq 5})$$

$$\ln \dot{\epsilon} = n \ln[\sinh(\alpha\sigma)] + \ln A - Q/(RT) \quad (\text{Eq 6})$$

The peak stress that signifies the highest load during high-temperature compression and is a function of the deformation condition is selected for estimating the corresponding strain (Ref 26). Equations 4-6 represent linear relationships between  $\ln \dot{\epsilon} - \ln \sigma$ ,  $\ln \dot{\epsilon} - \sigma$  and  $\ln \dot{\epsilon} - \ln(\sinh(\alpha\sigma))$ , and the values of  $n_1$ ,  $\beta$ , and  $n$  can be derived from the slope of the fitted lines from the above plots in the temperature range of 1050-1200 °C (Fig. 4). Further,  $\alpha$  can be calculated from the relation  $\alpha = \beta/n_1$  and the average value  $\alpha$  and  $n$  are considered as optimum for a given strain (Ref 46). The estimated result of material constants is given in Table 2.

Further, the correlation between flow stress and the strain rate could be presented based on linear regression corresponding to the hyperbolic sine relationship.

**Table 2** Estimated values of material constants and activation energy for a given strain at peak stress

$\alpha$ , MPa <sup>-1</sup>	$\beta$ , MPa <sup>-1</sup>	$n_1$	$n$	$Q$ , kJ/mol	$\ln A$
0.0051	0.0977	18.9227	6.9557	624	34.70

$$\ln \dot{\epsilon} = 6.64 \ln[\sinh(0.00418\sigma)] - 4.1494 \quad \text{for } T = 1323 \text{ K}$$

$$\ln \dot{\epsilon} = 6.49 \ln[\sinh(0.00493\sigma)] - 2.7013 \quad \text{for } T = 1373 \text{ K}$$

$$\ln \dot{\epsilon} = 7.22 \ln[\sinh(0.00541\sigma)] - 1.8078 \quad \text{for } T = 1423 \text{ K}$$

$$\ln \dot{\epsilon} = 6.95 \ln[\sinh(0.00616\sigma)] - 0.43846 \quad \text{for } T = 1473 \text{ K}$$

The activation energy for hot deformation is assumed to remain constant for small temperature ranges at which the strain rate is constant (Ref 42, 46). Further, Eq 6 can be rearranged for all the stress levels as follows:

$$n \ln[\sinh(\alpha\sigma)] = \ln \dot{\epsilon} + Q/(RT) - \ln A \quad (\text{Eq 7})$$

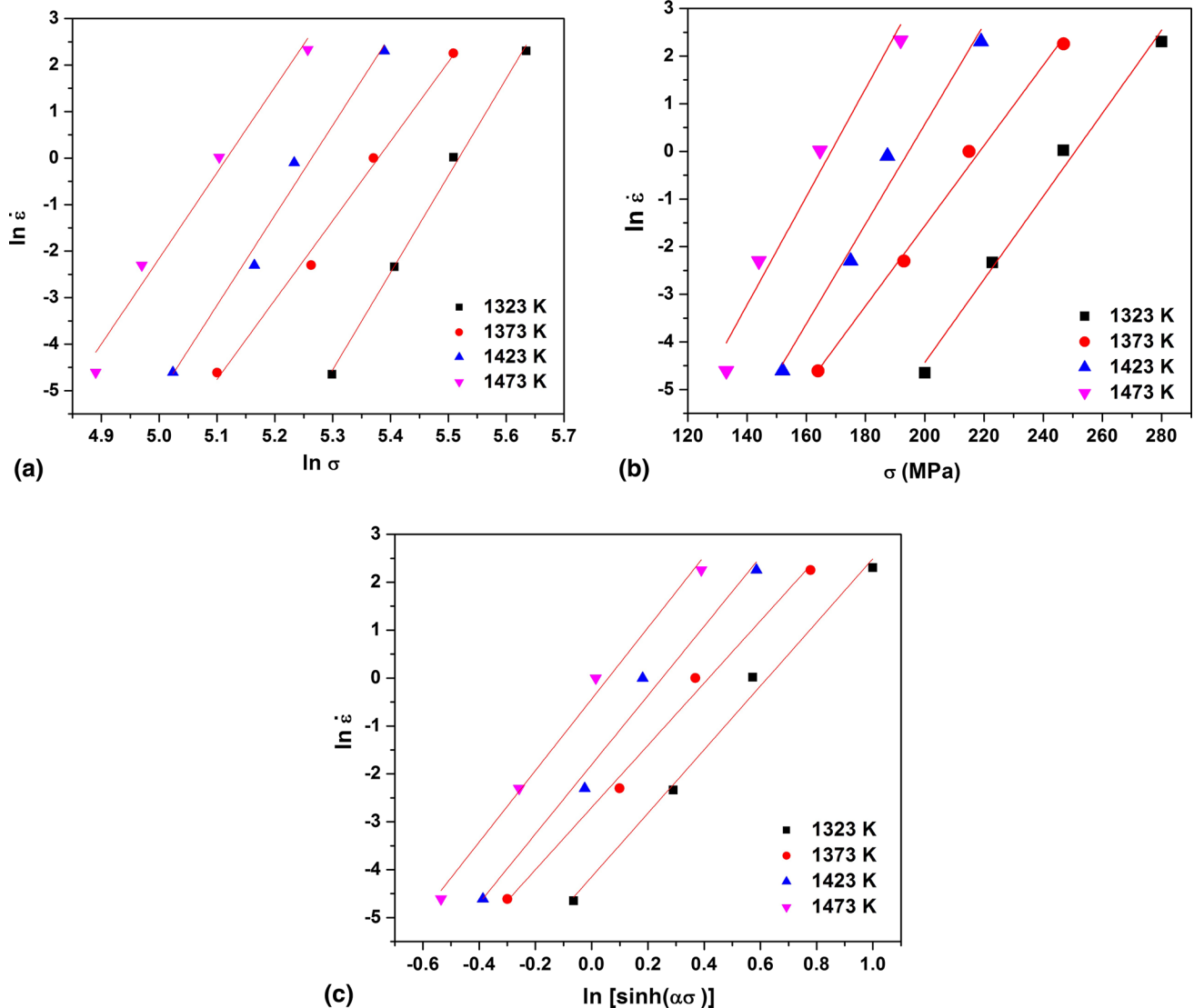


**Fig. 4** Relationship between (a)  $\ln \dot{\epsilon} - \ln \sigma$ , (b)  $\ln \dot{\epsilon} - \sigma$  and (c)  $\ln \dot{\epsilon} - \ln(\sinh(\alpha\sigma))$  of 18Cr ODS ferritic steel in a temperature range of 1323-1473 K

The activation energy can then be calculated from the slope of the plot that can be derived from the intercept of  $n \ln(\sinh(x\sigma))$  versus  $\ln \dot{\epsilon}$  as a function of  $1/T$ ; further, the intercept gives the value of  $\ln A$  (Ref 42, 46). The estimated  $Q$  value and  $\ln A$  for the 18Cr ODS steel is  $\sim 624$  kJ/mol and 34, respectively, in the temperature range of 1323-1473 K in the strain rate range of  $0.001-1 \text{ s}^{-1}$ . The estimated  $Q$  value is higher than that reported for non-ODS T24 ferritic steel (515 kJ/mol) (Ref 42). The higher values can be attributed to the dislocation pinning by the dispersoids which introduces a threshold stress for deformation.

During the initial stage of deformation, the dispersoids induce elastic stress through lattice mismatch within the matrix that restricts dislocation motion. The movement of dislocations is also restricted through the pinning effect, which causes dislocation sliding and climbing with increase in strain energy; increases in strain energy effect the dynamic recovery (Ref 26). In addition, the dispersoids also inhibit recrystallization by obstructing the formation of grain boundary and their advancement which attributes to delay in recrystallization phenomena. Besides, the reduction of grain boundary strength at high temperature promotes grain refinement and helps the material to deform easily, which outweighs the recrystallization phenomena.

Taking into account for the values of  $a$ ,  $Q$ ,  $A$ , and  $n$  into Eq 3, the constitutive equation of 18Cr ODS steel can be turned out to be:

$$\dot{\epsilon} = [\sinh(0.00517\sigma)]^{6.955} \exp(34.70 - 624/RT) \quad (\text{Eq 8})$$

### 3.4 Processing Map Generation

A dynamic material model (DMM), which considers the basic concepts for a large plastic flow with the conjunction of both continuum mechanics (Ref 47) and irreversible thermodynamics (Ref 48) reliably predicts (Ref 49, 50) the various workability regimes for a given material and processing map can be arrived at. According to the governing principle, the power dissipation ( $P$ ) from the workpiece during hot working is harmonized by two complementary components  $G$  and  $J$  as per the following equation:

$$P = \sigma \bullet \dot{\epsilon} = \int_0^{\dot{\epsilon}} \sigma \bullet d\dot{\epsilon} + \int_0^{\sigma} \dot{\epsilon} \bullet d\sigma = G + J \quad (\text{Eq 9})$$

where  $\sigma$  is the flow stress and  $\dot{\epsilon}$  is the strain rate. Further,  $G$  corresponds to power component which is dissipated during plastic deformation and  $J$  signifies the dissipation of power component that leads to evolution of microstructure via dynamic recovery/recrystallization (Ref 26, 30). The order of strain rate at a given temperature influences the power dissipation, which can be described by the constitutive material flow properties and the strain rate sensitivity  $m$  (Ref 26).

$$m = \left( \frac{d(\ln \sigma)}{d(\ln \dot{\epsilon})} \right) = \frac{dJ}{dG} \quad (\text{Eq 10})$$

Further, the efficiency of power dissipation ( $\eta$ ) which specifies the workability of the material at different domains of temperature and strain rate can be defined by (Ref 26):

$$\eta = \frac{J}{J_{\max}} = \frac{2m}{m+1} \quad (\text{Eq 11})$$

In addition, the instability parameter ( $\zeta(\dot{\epsilon})$ ) which imply the unstable region can be related to the strain rate and strain rate sensitivity by the relation (Ref 26):

$$\zeta(\dot{\epsilon}) = \frac{d\left(\ln \frac{m}{m+1}\right)}{d(\ln \dot{\epsilon})} + m \quad (\text{Eq 12})$$

The processing domain falls in the instability region if ( $\zeta(\dot{\epsilon}) < 0$ ) (Ref 26, 50) and the instability map is obtained from the plot of change in efficiency of power dissipation at different temperatures and strain rates. The workability regimes are separated with a contour value ( $\zeta(\dot{\epsilon}) = 0$ ). The flow stress at a finer step size has been calculated through the cubic spline interpolation to improve reliability and for each step size the strain rate sensitivity ( $m$ ), efficiency of power dissipation ( $\eta$ ) and instability parameter ( $\zeta(\dot{\epsilon})$ ) are determined from Eq 10, 11 and 12, respectively.

Figure 5 shows the distribution of strain rate sensitivity ( $m$ ) map with respect to temperature and strain rate. The variation of  $m$  in the entire range of temperatures and strain rates employed in this study is found to be within the range of 0.06-0.25. Similarly  $\eta$  and ( $\zeta(\dot{\epsilon})$ ) contour maps were also generated for all temperatures and strain rates. The processing map of 18Cr ODS ferritic steel is generated by superimposing the  $\eta$  and ( $\zeta(\dot{\epsilon})$ ) contour maps and is shown in Fig. 6, which reveals a limited safe workability regime (marked yellow) for processing this material. It is also observed that an instability domain exists in the temperature range of 1300-1473 K with strain rate  $> 1 \text{ s}^{-1}$  and 1330-1425 K with a strain rate  $> 0.1 \text{ s}^{-1}$ . The stored energy increases during deformation at high strain rate, since it is not rapidly distributed throughout the matrix due to localized deformed regions. This leads to thermoplastic/flow instability domain at higher ( $> 1$ ) strain rates for this steel (Ref 51). The safe temperature and strain rate domains of processing the steel are identified to lie between  $0.01$  and  $1 \text{ s}^{-1}$  at 1323 and 1473 K (circled in Fig. 4), which is also evident from the strain rate sensitivity map (Fig. 5) where the  $m$  values are very high. It is also observed that at a low strain rate of  $0.01 \text{ s}^{-1}$ , the dominant mechanism for the material flow behavior changes from dynamic recovery at 1300 K to dynamic recrystallization

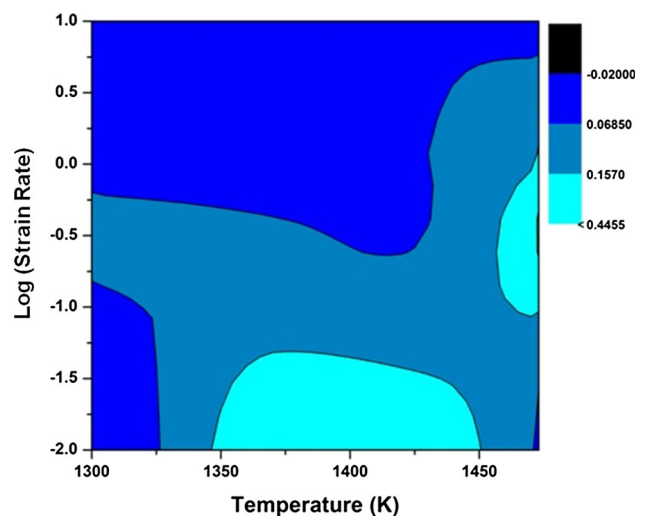
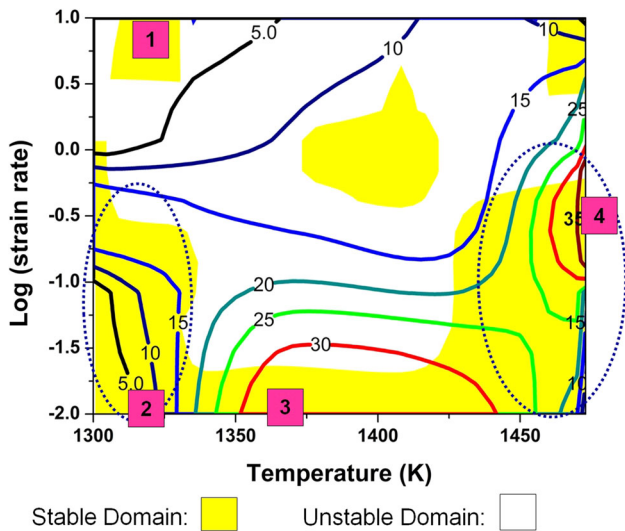


Fig. 5 Variation of strain rate sensitivity with temperature and strain rate for 18Cr-ODS ferritic steel



**Fig. 6** Processing map generated for 18Cr ODS ferritic steel at 0.5 true strain (\*region marked 1, 2, 3 and 4 are selected for microstructure analysis)

at 1450 K. These results are in agreement with the reported temperatures for the recovery and recrystallization as 1323 K and above 1423 K, respectively (Ref 27), in ODS ferritic steels, where the dispersoid distribution favors higher dislocation pinning during deformation.

Though the processing map indicates a safe domain at 1323 K at a strain rate  $10 \text{ s}^{-1}$ , the  $\eta$  contour value is low and also the domain size is small, suggesting that it is not energy efficient. Hence, the most favorable processing parameters are found to be between the temperature range of 1350-1450 K with a strain rate of  $0.01 \text{ s}^{-1}$  and 1473 K with a strain rate  $0.1 \text{ s}^{-1}$ , based on high values of peak efficiency ( $\eta$ ) up to 30-35% in the safe workability domain.

### 3.5 Evolution of Microstructure and Microtexture During Hot Compression Testing

The safe zone in processing map with respect to temperature and strain rate has been identified. However, this needs to be validated in conjunction with a detailed microstructure analysis. Hence, 4 regions in the safe zone (marked in Fig. 6) of the processing map have been selected for detailed analysis. Region 1 corresponds to high strain rate and low-temperature zone, Region 2 corresponds to low strain rate and temperature zone, while regions 3 and 4 lie in the high-efficiency safe zones. The resultant room temperature microstructures from these four regions are shown in Fig. 7(a, c, e and g). Significant differences are observed in Fig. 5 from the initial extruded microstructure (Fig. 1). Figure 5(a) shows the microstructure from region 1 corresponding to the steel deformed at 1323 K with strain rate of  $10 \text{ s}^{-1}$ . Elongated grains (aspect ratio  $> 1$ ) typical of a deformation induced microstructure is evident from the figure. A closer look at Fig. 7(a) indicates the coalescence of the initial fine bamboo-like structure of the extruded steel. The low-angle boundaries between the grains have been marked to indicate the retention of the deformed microstructure. Low ductility and low efficiency ( $\sim 5\%$ ) during deformation in this region is also evident from the lower strain rate sensitivity. The microstructure of the steel tested at 1323 K with strain rate of  $0.01 \text{ s}^{-1}$  from the safe domain (region 2) is shown in

Fig. 7(c). The microstructure reveals shear bands developed during deformation and initiation of fine recrystallized microstructure at the periphery of shear bands. Hence, it can be concluded that deformation at low temperatures and low strain rates leads to dynamic recovery which softens the material and average efficiency of up to 15% is achieved. Since the temperature is not high enough to compensate for the strengthening effect due to dislocation pinning by the dispersoids this region is prone to develop shear bands (Ref 52). With further increase in temperature from 1323 to 1423 K with strain rate  $0.01 \text{ s}^{-1}$  (region 3) the average efficiency and strain rate sensitivity increases from 5 to 30% and 0.068 to  $> 0.157$ , respectively. The microstructure corresponding to this region is given in Fig. 7(e) which shows equiaxed grain morphology, suggesting that dynamic recrystallization is the key mechanism that associated with deformation in this domain. A similar workability region is also observed at 1473 K with strain rate of  $0.1 \text{ s}^{-1}$  and the corresponding microstructure is shown in Fig. 7(g). This microstructure also reveals an equiaxed microstructure with slightly coarser grains due to higher temperature and strain rate in contrast to the specimen deformed at a strain rate of  $0.01 \text{ s}^{-1}$  at 1373 K. This shows that dynamic recrystallization with partial grain growth is dominant in this domain during deformation as shown in Fig. 8 compares the frequency distribution of grain size in these four regions. The analysis shows that low-temperature deformation phenomena result in a large variation in grain size distribution due to coalescence of grains during the deformation process. Dynamic recrystallization is favored during deformation at temperatures around 1373 K for low strain rates below rate  $10^{-2} \text{ s}^{-1}$  while at high temperatures  $> 1423 \text{ K}$  it is observed even at high strain rate of  $10^{-1} \text{ s}^{-1}$ . The resultant microstructure consists of nearly uniform fine-sized (2-3  $\mu\text{m}$ ) grains wherein the pinning effect of the dispersoids effectively restricts the grain growth despite high temperatures.

Figure 7(b, d, f and h) shows the inverse pole figure maps corresponding to the same 4 regions of discussed above, which reveals the texture evolution during hot compression. During uniaxial deformation, the fiber texture is typically represented using inverse pole figures to truly represent the tendency for preferred crystallographic directions with respect to particular sample axis. It is observed that there is significant reduction from 8.1 to 2.3 of  $\langle 110 \rangle$  fiber texture of the extruded steel after deformation at strain rate of  $10 \text{ s}^{-1}$  at 1323 K (Fig. 7(b)). The retention of directional microstructure at this test temperature reflects efficient pinning effect of dispersoids while also restricting boundary migration (Ref 52). Also, the decrease in  $\langle 110 \rangle$  fiber texture during hot deformation through the uniaxial compression of metals, can be understood based on grain coalescence due to the reversal of direction of deformation (Ref 53). However, at the same temperature of 1323 K, when the strain rate is reduced from 10 to  $0.01 \text{ s}^{-1}$  the fiber texture along  $\langle 110 \rangle$  changes to predominantly  $\langle 100 \rangle$  with small contribution from  $\langle 111 \rangle$  as shown in Fig. 7(d).

Shearing as well as partial recrystallization is responsible for the development of a double fiber texture during plastic deformation at 1323 K at low strain rate of  $0.01 \text{ s}^{-1}$ , which is reported as characteristic of bcc alloys (Ref 31). Figure 7(f) shows the IPF maps corresponding to region 3 with deformation at 1373 K at a low strain rate  $0.01 \text{ s}^{-1}$ , which reveals the development of  $\langle 111 \rangle$  fiber without any signature of  $\langle 110 \rangle$ . It is also observed in Fig. 7(h) that there is no appreciable change in texture when the compressive deformation temperature and

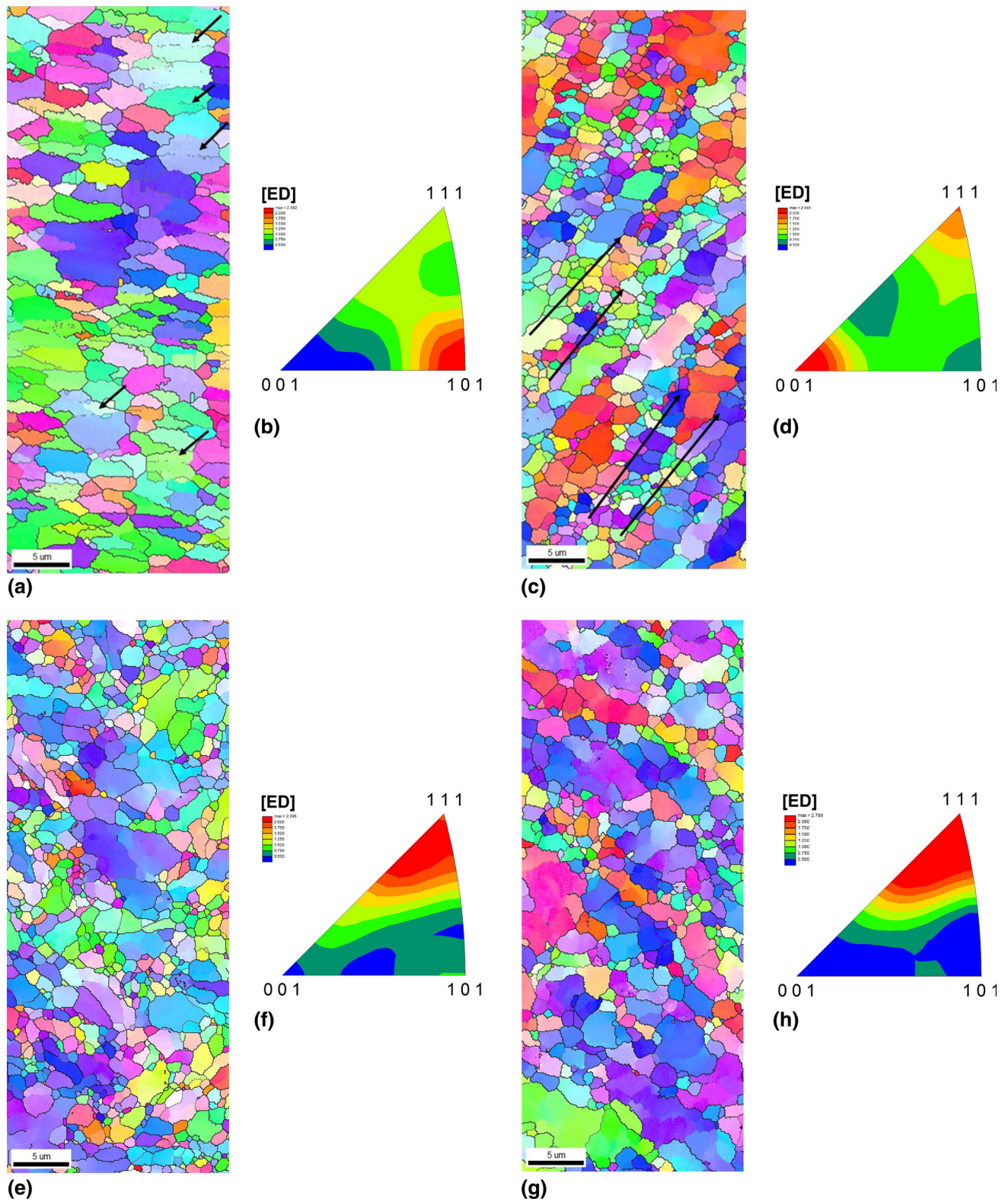


**Fig. 7** EBSD crystal orientation map of zone (a) 1, (c) 2, (e) 3 and (f) 4 as marked in Fig. 6. and corresponding inverse pole figures intensity distribution of zone (b) 1, (d) 2, (f) 3 and (h) 4, respectively, with respect to extrusion direction

strain rate is increased to 1473 K and  $0.1 \text{ s}^{-1}$ , respectively. This clearly indicates that the preferential  $\langle 111 \rangle$  texture along the deformation direction is responsible for the dynamic recrystallization during deformation in both these cases. However, dynamic recrystallization occurs through progressive

subgrain rotation at 1373 K with strain rate of  $0.01 \text{ s}^{-1}$ . However, both cases involve strain-induced phenomenon with limited or no movement of high-angle boundaries at 1473 K (Ref 31). The relevant texture components which evolve during high-temperature deformation of ferritic steels are often



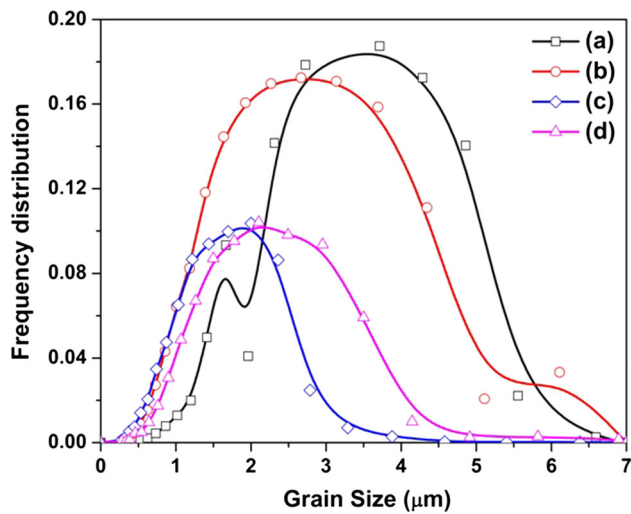


**Fig. 8** Grain size distribution of respective deformation mode of zone (a) 1, (c) 2, (e) 3 and (f) 4 as marked in Fig. 6

reported to be  $\alpha$ -fibers ( $\{110\}$ //RD),  $\gamma$ -fibers ( $\langle 111 \rangle$ //ND) and  $\theta$ -fibers  $\langle 100 \rangle$ //ND (Ref 54). Hence, comparison of the IPFs in the present study confirms the following:

- (a) Formation of  $\theta$ -fiber during deformation at 1323 K with strain rate of  $0.01 \text{ s}^{-1}$  due to shearing mechanism, and
- (b) Formation of  $\gamma$ -fiber during deformation at 1373 K with strain rate of  $0.01 \text{ s}^{-1}$  and 1473 K with strain rate  $< 0.1 \text{ s}^{-1}$  due to dynamic recrystallization.

## 4. Conclusions

The optimum high-temperature workability region has been identified for 18Cr Cr oxide dispersion strengthened ferritic steel based on dynamic material model approach using the results obtained from the hot isothermal compression tests in a wide range of temperatures (1323-1473 K) and strain rates ( $0.01$ - $10 \text{ s}^{-1}$ ). The variation in microstructure and microtexture at different safe domains of processing map are analyzed. The following important conclusions are drawn from this investigation.

- (A.) Limited safe processing domains have been identified based on the influence of strain rate sensitivity ( $m$ ), efficiency of power dissipation ( $\eta$ ) and instability parameter ( $\xi(\dot{\epsilon})$ ) parameters.
- (B.) Instability domains have been identified in the temperature range of 1323-1423 K with strain rate  $> 0.1 \text{ s}^{-1}$ .
- (C.) Based on superior workability region with peak efficiency up to 30-35%, the most favorable processing parameters have been optimized in the temperature range of 1350-1450 K with a strain rate of  $0.01 \text{ s}^{-1}$  and 1473 K with a strain rate  $0.1 \text{ s}^{-1}$ .
- (D.) Low-efficiency parameter in the safe processing domain resulted in shearing and retention of deformed microstructure at high strain rate ( $10 \text{ s}^{-1}$ ) and low strain rates ( $0.01 \text{ s}^{-1}$ ), respectively, and a higher grain

size distribution is attributed to coalescence of grains during deformation.

- (E.) High-temperature compression minimizes the  $\langle 110 \rangle$  fiber texture; At 1373 K with strain rate  $< 0.01 \text{ s}^{-1}$  and at 1473 K with a strain rate of  $< 0.1 \text{ s}^{-1}$   $\langle 111 \rangle$  fiber texture is obtained.

## Acknowledgments

The authors would like to thank Dr. G. Amarendra, Director, Metallurgy and Materials Group and Dr. A. K. Bhaduri, Director, Indira Gandhi Centre for Atomic Research for their sustained support and encouragement during this work. The authors thank Nuclear Fuel Complex (NFC), Hyderabad, for the hot extruded samples. They also thank Dept. of MME, IIT-Madras, Chennai, for providing the Gleeble simulator facility for uniaxial compression testing and UGC-DAE-CSR at Kalpakkam for extending the FEG-SEM facility.

## References

1. K.L. Murty and I. Charit, Structural Materials for Gen-IV Nuclear Reactors: Challenges and Opportunities, *J. Nucl. Mater.*, 2008, **383**, p 189-195
2. A. Aitkaliyeva, L. He, H. Wen, B. Miller, X.M. Bai, and T. Allen, Irradiation Effects in Generation IV Nuclear Reactor Materials, *Structural Materials for Generation IV Nuclear Reactors*, chap. 7, Elsevier, Amsterdam, 2017, p 253-283
3. V. de Castro, E.A. Marquis, S.L. Perez, R. Pareja, and M.L. Jenkins, Stability of Nanoscale Secondary Phases in an Oxide Dispersion Strengthened Fe-12Cr Alloy, *Acta Mater.*, 2001, **59**, p 3927-3936
4. P. Dubuisson, Y. de Carlan, V. Garat, and M. Blat, ODS Ferritic/Martensitic Alloys for Sodium Fast Reactor Fuel Pin Cladding, *J. Nucl. Mater.*, 2012, **428**, p 6-12
5. R.L. Klueh, Elevated Temperature Ferritic and Martensitic Steels and Their Application to Future Nuclear Reactors, *Int. Mater. Rev.*, 2005, **50**, p 287-312
6. S. Ukai, M. Harada, H. Okada, M. Inoue, S. Nomura, S. Shikakura, K. Asabe, T. Nishida, and M. Fujiwara, Alloying Design of Oxide Dispersion Strengthened Ferritic Steel for Long Life FBRs Core Materials, *J. Nucl. Mater.*, 1993, **204**, p 65-73
7. S. Ukai and M. Fujiwara, Perspective of ODS Alloys Application in Nuclear Environments, *J. Nucl. Mater.*, 2002, **307-311**, p 749-757
8. C. Cayron, E. Rath, I. Chu, and S. Launois, Microstructural Evolution of  $\text{Y}_2\text{O}_3$  and  $\text{MgAl}_2\text{O}_4$  ODS EUROFER steels During Their Elaboration by Mechanical Milling and Hot Isostatic Pressing, *J. Nucl. Mater.*, 2004, **335**, p 83-102
9. A. Alamo, J.L. Bertin, V.K. Shamardin, and P. Wident, Mechanical Properties of 9Cr Martensitic Steels and ODS-FeCr Alloys After Neutron Irradiation at 325 °C up to 42 dpa, *J. Nucl. Mater.*, 2007, **367-370**, p 54-59
10. H. Hadraba, B. Fournier, L. Stratil, J. Malaplate, A.L. Rouffié, P. Wident, L. Ziolk, and J.L. Béchade, Influence of Microstructure on Impact Properties of 9-18%Cr ODS Steels for Fusion/Fission Applications, *J. Nucl. Mater.*, 2011, **411**, p 112-118
11. T. Tanno, M. Takeuchi, S. Ohtsuka, and T. Kaito, Corrosion Behavior of ODS Steels with Several Chromium Contents in Hot Nitric Acid Solutions, *J. Nucl. Mater.*, 2017, **494**, p 219-226
12. Z. Oksiuta, High-Temperature Oxidation Resistance of Ultrafine-Grained 14%Cr ODS Ferritic Steel, *J. Mater. Sci.*, 2013, **48**, p 4801-4805
13. R. Novotny, P. Janik, S. Penttila, P. Hahner, J. Macak, J. Siegl, and P. Haüsild, High Cr ODS Steels Performance Under Supercritical Water Environment, *J. Supercrit. Fluids*, 2013, **81**, p 147-156
14. A. García-Junceda, M. Hernández-Mayoral, and M. Serrano, Influence of the Microstructure on the Tensile and Impact Properties of a 14Cr ODS Steel Bar, *Mater. Sci. Eng. A*, 2012, **556**, p 696-703

15. S. Ukai, S. Mizuta, T. Yoshitake, T. Okuda, M. Fujiwara, S. Hagi, and T. Kobayashi, Tube Manufacturing and Characterization of Oxide Dispersion Strengthened Ferritic Steels, *J. Nucl. Mater.*, 2000, **283–287**, p 702–706
16. M.J. Alinger, G.R. Odette, and G.E. Lucas, Tensile and Fracture Toughness Properties of MA957: Implications to the Development of Nanocomposited Ferritic Alloys, *J. Nucl. Mater.*, 2002, **307**, p 484–489
17. M. Wang, Z. Zhou, H. Sun, H. Hu, and S. Li, Microstructural Observation and Tensile Properties of ODS-304 Austenitic Steel, *Mater. Sci. Eng. A*, 2013, **559**, p 287–292
18. Z. Oksiuta, P. Mueller, and P. Spatig, Effect of Thermo-mechanical Treatments on the Microstructure and Mechanical Properties of an ODS Ferritic Steel, *J. Nucl. Mater.*, 2011, **412**, p 221–226
19. D. Samantaray, S. Mandal, C. Phaniraj, and A.K. Bhaduri, Flow Behavior and Microstructural Evolution During Hot Deformation of AISI, Type 316 L(N) Austenitic Stainless Steel, *Mater. Sci. Eng. A*, 2011, **528**, p 8565–8572
20. T. Seshacharyulu, S.C. Medeiros, W.G. Frazier, and Y.V.R.K. Prasad, Microstructural Mechanisms During Hot Working of Commercial Grade Ti-6Al-4V with Lamellar Starting Structure, *Mater. Sci. Eng. A*, 2002, **325**, p 112–125
21. L.J. Huang, L. Geng, A.B. Li, X.P. Cui, H.Z. Li, and G.S. Wang, Characteristics of Hot Compression Behavior of Ti-6.5Al-3.5Mo-1.5Zr-0.3Si Alloy with an Equiaxed Microstructure, *Mater. Sci. Eng. A*, 2009, **505**, p 136–143
22. S. Venugopal, S.L. Mannan, and Y.V.R.K. Prasad, Processing Map for Cold and Hot Working of Stainless Steel Type AISI, 304 L, *Mater. Lett.*, 1992, **15**, p 79–83
23. S. Venugopal, S.L. Mannan, and Y.V.R.K. Prasad, Processing Maps for Hot Working of Commercial Grade Wrought Stainless Steel type AISI, 304, *Mater. Sci. Eng. A*, 1994, **177**, p 143–149
24. P.V. Sivaprasad, S. Venugopal, V. Maduraimuthu, M. Vasudevan, S.L. Mannan, Y.V.R.K. Prasad, and R.C. Chaturvedi, Validation of Processing Maps for a 15Cr-15Ni-2.2Mo-0.3Ti Austenitic Stainless Steel Using Hot Forging and Rolling Tests, *J. Mater. Process. Technol.*, 2003, **132**, p 262–268
25. P.V. Sivaprasad, S.L. Mannan, and Y.V.R.K. Prasad, Identification of Optimum Process Parameters for Hot Extrusion Using Finite Element Simulation and Processing Maps, *Mater. Sci. Technol.*, 2004, **20**, p 1545–1550
26. G. Zhang, Z. Zhou, H. Sun, L. Zou, M. Wang, and S. Li, Hot Deformation Behavior and Processing Map of a 9Cr Ferritic/Martensitic ODS Steel, *J. Nucl. Mater.*, 2014, **455**, p 139–144
27. T. Narita, S. Ukai, T. Kaito, S. Ohtsuka, and T. Kobayashi, Development of Two-Step Softening Heat Treatment for Manufacturing 12Cr-ODS Ferritic Steel Tubes, *J. Nucl. Sci. Technol.*, 2012, **41**, p 1008–1012
28. M. Nagini, R. Vijay, K.V. Rajulapati, K.B. Rao, M. Ramakrishna, A.V. Reddy, and G. Sundararajan, Effect of Process Parameters on Microstructure and Hardness of Oxide Dispersion Strengthened 18Cr Ferritic Steel, *Met. Trans. A*, 2016, **47**, p 4197–4209
29. Y. Li, E. Onodera, and A. Chiba, Evaluation of Friction Coefficient by Simulation in Bulk Metal Forming Process, *Met. Trans. A*, 2010, **51**, p 1210–1215
30. D. Samantaray, S. Mandal, and A.K. Bhaduri, Optimization of Hot Working Parameters for Thermo-mechanical Processing of Modified 9Cr-1Mo (P91) Steel Employing Dynamic Materials Model, *Mater. Sci. Eng. A*, 2011, **528**, p 5204–5211
31. B. Verlinden, J. Driver, I. Samajhdar, and R.D. Doherty, *Thermo-mechanical Processing of Metallic Material*, Elsevier, London, 2007
32. J.J. Sidor, K. Verbeken, E. Gomes, J. Schneider, P.R. Calvillo, and L.A.I. Kestens, Through Process Texture Evolution and Magnetic Properties of High Si Non-oriented Electrical Steels, *Mater. Character.*, 2012, **71**, p 49–57
33. F.J. Humphreys and M. Hatherly, *Recrystallization and Related Annealing Phenomena*, Elsevier, London, 1995
34. C.L. Chen, G.J. Tatlock, and A.R. Jones, Effect of Annealing Temperatures on the Secondary Re-crystallization of Extruded PM2000 Steel Bar, *J. Microsc.*, 2009, **233**, p 474–481
35. M. Serrano, M. Hernández-Mayoral, and A. García-Junceda, Microstructural Anisotropy Effect on the Mechanical Properties of a 14Cr ODS Steel, *J. Nucl. Mater.*, 2012, **428**, p 103–109
36. E.I. Poliakt and J.J. Jonass, One-Parameter Approach to Determining the Critical Conditions for the Initiation of Dynamic Recrystallization, *Acta Mater.*, 1996, **44**, p 127–136
37. A. Sarkar, A. Marchattiar, J.K. Chakravarty, and B.P. Kashyap, Kinetics of Dynamic Recrystallization in Ti-Modified 15Cr-15Ni-2Mo Austenitic Stainless Steel, *J. Nucl. Mater.*, 2013, **432**, p 9–15
38. G.V. Prasad, M. Goerdeler, and G. Gottstein, Work Hardening Model Based on Multiple Dislocation Densities, *Mater. Sci. Eng. A*, 2005, **400**, p 231–233
39. A.D. Rollett and U.F. Kocks, A Review of the Stages of Work Hardening, *Solid State Phenom.*, 1993, **35(36)**, p 1–9
40. E.I. Poliakt and J.J. Jonas, Initiation of Dynamic Recrystallization in Constant Strain Rate Hot Deformation, *ISIJ Int.*, 2003, **43**, p 684–691
41. C.M. Sellars and W.J. McTegart, On the Mechanism of Hot Deformation, *Acta Metal.*, 1966, **14**, p 1136–1138
42. H. Li, D. Wei, J. Hua, Y. Li, and S. Chen, Constitutive Modeling for Hot Deformation Behavior of T24 Ferritic Steel, *Comput. Mater. Sci.*, 2012, **53**, p 425–430
43. H. Takuda, H. Fujimoto, and N. Hatta, Modelling on Flow Stress of Mg-Al-Zn Alloys at Elevated Temperatures, *J. Mater. Proc. Technol.*, 1998, **80–81**, p 513–516
44. A. Galiyev, R. Kaibyshev, and T. Saikai, Continuous Dynamic Recrystallization in Magnesium Alloy, *Mater. Sci. Forum*, 2003, **419–422**, p 509–514
45. T. Sakai and J.J. Jonas, Strength and Structure Under Hot-Working Conditions, *Acta Mater.*, 1984, **32**, p 189–209
46. D. Samantaray, S. Mandal, and A.K. Bhaduri, Constitutive Analysis to Predict High-Temperature Flow Stress in Modified 9Cr-1Mo (P91) Steel, *Mater. Design*, 2010, **31**, p 981–984
47. H. Ziegler, I.N. Sneddon, and R. Hill, Ed., *Progress in Solid Mechanics*, Wiley, New York, 1965, p 91–193
48. I. Prigogine, Time, Structure and Fluctuations, *Science*, 1978, **201**, p 777–785
49. Y. Prasad, Processing Maps: A Status Report, *J. Mater. Eng. Perform.*, 2003, **12(6)**, p 638–645
50. Y. Prasad and T. Seshacharyulu, Modelling of Hot Deformation for Microstructural Control, *Int. Mater. Rev.*, 1998, **43**, p 243–258
51. L. Wang, Y. Fan, and G. Huang, Plastic Deformation at Elevated Temperature and Processing Maps of Magnesium Alloy, *Chin. J. Nonferrous Met.*, 2004, **14(7)**, p 1068–1072
52. T.S. Chou and H.K.D.H. Bhadeshia, Grain Control in Mechanically Alloyed Oxide Dispersion Strengthened MA957 Steel, *Mater. Sci. Technol.*, 1993, **9**, p 890–897
53. M. G. Stout, J. S. Kallend, U.F. Kocks, M. A. Przystupa and A. D. Rollet, in *Proceedings on 8 International Conference on Textures of Materials*, J.S. Kallend and G. Gottstein, Eds., TMS, Warrendale, 1988, p 479–484
54. B. Sander and D. Raabe, Texture Inhomogeneity in a Ti-Nb-Based  $\beta$ -Titanium Alloy After Warm Rolling and Recrystallization, *Mater. Sci. Eng. A*, 2008, **479**, p 236–247